

建築水資源與給排水期刊

Journal of Water Resource, Supply and Drainage for Buildings

中華民國 104 年 2 月出版

創刊號

要 目

- ⊙ **Hydrodynamic performances of gully with air-water flows in drainage system**
- ⊙ 全球暖化對台灣未來水資源之影響評估

建築水資源與給排水期刊

Journal of Water Resource, Supply and Drainage for Buildings

創刊號

社團法人台灣給水排水研究學會

中華民國 104 年 2 月

建築水資源與給排水期刊

Journal of Water Resource, Supply and Drainage for Buildings

目 錄

- 1. Hydrodynamic performances of gully with air-water flows in drainage system 1**
- S.W. Chang Department of Marine Engineering, National
 Kaohsiung Marine University, Taiwan
- D.C. Lo Department of Maritime Information and Technology,
 National Kaohsiung Marine University, Taiwan
- H.F. Liu CU Golden Power Products, Inc, Taiwan
- J.S. Liou Department of Maritime Information and Technology,
 National Kaohsiung Marine University, Taiwan
- 2. 全球暖化對台灣未來水資源之影響評估..... 21**
- 陳昭銘 國立高雄海洋科技大學海事資訊科技系
- 蔡雅琴 國立高雄海洋科技大學海事資訊科技系

Hydrodynamic performances of gully with air-water flows in drainage system

S.W. Chang* Department of Marine Engineering, National Kaohsiung Marine University,
Taiwan

D.C. Lo Department of Maritime Information and Technology, National Kaohsiung
Marine University, Taiwan

H.F. Liu CU Golden Power Products, Inc, Taiwan

J.S. Liou Department of Maritime Information and Technology, National Kaohsiung
Marine University, Taiwan

* Corresponding author email: swchang@mail.nkmu.edu.tw; Tel: +886-7-8100888ext.5216

(Received 21th February 2014, accepted 31th March 2014)

Abstract

This study examines the hydrodynamic performances of a gully designed for building drainage system. The transient variations of free surface, fluid velocity and static pressure in the gully with twin air-water inlets are numerically analyzed by adopting turbulence model(s) to attack the moving boundary problem. Experimental test results reconfirm the numerical predications with the maximum capacities and the oscillating airflow pressures detected. Flow images illustrating the interfacial air-water flow structures at various test conditions are presented.

Particularly, as an attempt to improve the measurement quality for the self-depuration capacity specified in EN 1253-2:2002, which has been widely adopted as the international standard for testing the hydrodynamic performance of gullies with building applications, the optical measurement method is newly devised and described in details. The favorable numerical and experimental results confirm the applicability of present gully in a modern drainage system for preventing odour transmissions.

Keywords: Hydrodynamics Air-water Two-phase Flow, Drainage, Building.

Nomenclature

English symbols

A	fractional flow areas (m^2)
b	flow losses in porous media or across porous baffle plates ($m s^{-2}$)
d	entry tube diameter (m)
f	viscous accelerations term ($m s^{-2}$)
G	acceleration rates of fluid particles ($m s^{-2}$)
L	lumen
P	static pressure (Pa)
Q	volume flow rate ($L min^{-1}$)
Re_L	Reynolds number of liquid flow for mixed entry water = $\rho_L V_L d / \mu_L$
V_F	fractional flow volume ($m^3 s^{-1}$)
V_L	mean liquid flow velocity for mixed entry water ($m s^{-1}$)
u,v,w	fluid velocities in x,y,z direction ($m s^{-1}$)
x,y,z	coordinates (m)

Greek symbols

α	void fraction of entry flow
ρ_L	density of liquid flow for mixed entry water ($kg m^{-3}$)
μ	dynamic viscosity of liquid flow for mixed entry water ($kg s^{-1} m^{-1}$)

Subscripts

A	flow entry A
B	flow entry B

1.Introduction

Efficient transportation of mixed water from a variety of appliances connecting with the vertical stack in a building for a modern drainage system requires multi-discipline research efforts. As the mixed water flow in a drainage system involves complex air-water interfacial mechanisms, the sufficient discharging capacities with the capability of preventing the foul odors ingress into the habitable spaces within the allowable acoustic limits propose considerable challenge for the architecture designers. With random and intermittent falling water streams into the vertical stack via the discharge branches, the entrained airflow by the water stream yields the water discharge into the complex air-water two-phase flow taking a variety of interfacial patterns. The types of local interfacial flow structures for such mixed water are affected by the geometry of the pipe line/appliance, the flow rate of mixed water, the location where the appliance is installed and the type of discharge. In compliance with the design code of a drainage system, the common two-phase flow patterns in a branch and the stack are the stratified/wavy and the annular flows respectively. As the branch discharge is often a random and intermittent process, the stratified/wavy flows through a drainage system inherit the intermittent

characteristic as the transient phenomena [1]. Over the air-water interfaces, the air movements are induced by the interfacial shear forces on the free surfaces of the moving mixed water; which locally trigger the positive or negative transient air pressures and propagate through the stack and branches of the entire drainage system [2]. Moreover, the transient propagation of air pressures at sonic speed is affected by the local air-water interfacial structure and the reflection and transmission at the flow boundaries. Very complicate two-phase flow phenomena signify the hydrodynamic performances of a drainage system, which also determine the transient propagation of airflow pressures through the drainage network. Particularly, the blockage of a high momentum air stream by the water curtain or the water excursions in a drainage system often diminishes a trap seal due to the water hammer effect [3]. Nevertheless, the propagation of positive or negative transient pressures, which interdependently affect the interfacial structures and the airflow velocities, could cause unfavorable acoustic effect, limit the maximum discharge capacity and damage the trap seals in a drainage system.

To prevent foul odors ingress into the habitable spaces through the interconnected drainage network in a building, it is a common practice to install

the water seals at locations where appears as appropriate. However, triggered by the various and complex air-water interfacial actions along the interconnecting pipe works of a drainage system, the stimulated airflow pressure waves, which generally transmit at sonic speed, can damage these water seals. In this regard, the requirement for a trap seal with about 50mm water height is typical so that the permissible pressure excursions for a drainage system is generally determined as $\pm 375 \text{ Nm}^{-2}$ [1-2]. As an attempt to suppress the pressure surges in a drainage system, Swaffield et al [4] simulated the propagation of air pressure transients in the drainage system by solving the St. Venant equations using finite difference scheme; while the positive or negative pressure reflections at the interfacial boundaries were embodied in the airflow momentum equation via the friction coefficient to account the manifesting shearing drag in the airflow. Due to the complicate two-phase air-water flow phenomena in each appliance, branch, junction and the stack of a drainage system, the suppression of undesirable pressure transients through a drainage system remains as a formidable task. Particularly the influences of the various two-phase flow phenomena in each component and appliance of a drainage system on the hydrodynamic performances of a drainage system are interdependent. As a result,

various research works are motivated with their particular aims at optimizing the performances of the sub-assemblies in a drainage system with attendant innovative drainage components devised. In this respect, the vortex fin [3] was installed at the elbow bend of a vertical stack to stabilize the airflow pressures by suppressing the positive pressure surges caused by the water curtain downstream the middle section of the elbow-bend. As the water seal in a gully can prevent the transmission of odors ingress through the interconnected networks of a drainage system at any selected junction, several types of gully were patented [5-12] and tested for providing the stable water seal at a multiple junction in a drainage system. In [6], the hydrodynamic characteristics of a gully were reported using a set of numerical results. Within the framework of the lumped bubbly flow model, the geometries of entry/discharge ports and the plenum chamber of a gully were shown as the predominant factors determining the air-bubble dynamics and thus the oscillating pressures in a gully [6].

Relevant researches for the hydrodynamic performances and the associated air-water interfacial mechanisms in a gully are very rare [5, 15], leading to the insufficient revelation for the influences of gully geometry, entry void fraction of mixed water and the air-

water flow rate on its hydrodynamic performances. However, due to the widespread usages of gully in modern drainage systems for buildings, European Council has regulated EN 1253-2 standard [13] in 2002 for testing the hydrodynamic performances of a gully. In Gullies for buildings – Part 2: Test methods, the testing guidelines for load, water seal, blockage prevention, thermal behavior, tightness and flow rate are regulated [13]. Among the various test methods specified by EN 1253-2, the self-cleaning performance of a gully is tested by drifting solid spheres in the air-water flow through the gully. As water is the commonest solvent for many odor ingredients, the influence of localized small-scale recirculation zones in a gully, which impede the replenishment of fresh mixed water through a gully, on the self-depuration performance cannot be quantitatively identified. As an attempt to quantitatively assess the self-depuration performance of a gully, a newly devised optical testing method is presented with its testing characteristics examined. Using the patented triple-entry gully as an illustrating specimen, the test results determined from the newly devised optical assessment for self-depuration performance as well as the associated hydrodynamic performances of the gully are numerically and experimentally

examined.

2. Experimental and numerical details

2.1 Experimental facilities

Figure 1 depicts (a) test facilities with detailed illustrations for the optical device measuring the self-depuration performance (b) transparent test gully. As shown by Fig. 1(a), water fed from tank (1) which locates at fifth floor of a building to provide 13 m of water height is guided through a vertical stack (2) to the test gully (3). Complying with the design code for the single-pipe vertical stack in a building drainage system, an air admitting valve (4) is installed on top of the vertical stack. When water stream flows inside the vertical stack to entrain airflow in the drainage pipeline, the airflow pressure is controlled in the typical range of $\pm 375 \text{ Nm}^{-2}$ via the auto air entrainment through the air admitting valve (4). Similar to the practical conditions, the mixed water (air-water) flows are established prior to entering the test gully (3). Net volume of the water flow through the test gully (3) during a test period is measured by the downstream water tank (5) with the time span detected by the electronic timer. The method adopted to detect the water flow rate complies with the method of water flow rate measurement regulated by CNS14431 Q3001 [14]; which enables the

measurement of the averaged volume flow rate of water through the test gully (3). A scale is attached along the inner periphery of each transparent inlet pipe (6)(7) connecting with the test gully (3). As the stable stratified air-water flow in the basically horizontal inlet pipe (6)(7) is emulated by this test facility, the void fraction (α) of entry mixed water can be determined in according to the water level measured from each inlet pipe (6)(7). The air-water flow structures in the gully (3) at each tested Re_L with single and/or twin entry flows are visualized from the snapshots collected by the CCD image system (8). This imaging system can record the flow image at 300 fps with 600 pixels per gully width. The CCD camera (8) is aimed at the angle normal to the test gully (3) at a constant focal length. Locations of the light sources are individually adjusted for each test condition. As indicated in Fig. 1, the static airflow pressure is detected by a computerized digital micro manometer with the precision of 0.01 mm-H₂O (9). The pressure measurements are simultaneously performed with the flow visualization tests with the temporal variation of flow pressures detected/stored by the on-line data acquisition system. Depending on the sensing location and the hydrodynamic performance of the test gully (3), the agitating air bubbles and/or

pressure waves triggered by the unstable interfacial surface could stimulate pressure fluctuations. The detailed temporal variation of the airflow pressure at each test condition is recorded and stored by present measurement unit for analyzing the hydrodynamic performance of the test gully and validating the numerical results.

The constructional details of the of present test gully show several distinct features designed for improving the hydrodynamic performances, Fig. 1(b). This gully is configured by a cylindrical plenum chamber (1) within which a nozzle shaped core (2) directs the accelerated mixed water stream from the twin perpendicular inlet ports (3)(4) toward the inclined base (5). As depicted by Fig. 1(b), the inclination of base plate (5) is designed to guide the mixed water stream toward the exit port (6). Cross-section area of the exit port (6) is equal to the sectional annular area between the nozzle core (2) and the cylindrical outer casing (7). A filter leaf (8) is installed on the top of the gully assembly. Although such open contact with atmosphere adds another pathway for airflow entrainment, it remains as a common practice in many countries for discharging bathroom/kitchen waste water by fitting a filter leaf on the floor to connect with the drainage system. An optional segregation

plate (9) in the nozzle core (2) can also be installed to separated the mixed water streams from the two perpendicular inlet ports (3)(4). It is noticed that a streamlined bump (10) is installed at the base of the exit port (6). This design concept follows the typical practice for stabilizing the open channel flow upstream the bump installed on the river bank. The favorable impacts of the streamlined bump (10) for stabilizing the mixed water flow through present test gully will be later demonstrated using the experimental /numerical results.

To quantitatively assess the self-depuration performance for each test gully, the normalized lumen level through the test gully at each test condition is detected by present computerized optical system. As shown by Fig. 1(a), the light source emits light through the test gully, within which the mixed water flows, toward the optical receiver (10). The optical receiver (10) is positioned at the opposite side of the light source to transmit the received light signal to the PC via the converter (11). By way of feeding the mixed water at the particular test condition defined by Re_L and α , the reference lumen levels at the pure water flow condition (L_1) are initially detected. It is worth noting that the air bubbles emerging in the water trap of each test gully reflect light and affect the light deflection. Thus the instant lumen values

at the pure-water test conditions oscillate about L_1 reference and depend on the interfacial properties of the water trap in the test gully, which are geometry, Re_L and α dependent. However, the temporal lumen variations at the pre-defined pure mixed water (clean) entry conditions are detectable by present optical unit so that the L_1 references for the particular test gully are pre-determined. Prior to feeding the mixed water into the test gully for self-depuration performance test, the water trap stored in the test gully is dyed by the black ink with the lumen level (L_0) detected. With the same light source and optical receiving unit, the L_0 level at each “dark” test condition is controllable by adjusting the equivalent concentration of ink and appears as a stable reference due to the absence of air bubble prior to feeding the mixed water into the test gully. After charging the mixed water into the test gully, the lumen level starts rising from L_0 toward L_1 . The detailed temporal lumen variation from L_0 to L_1 represents the self-depuration performance of the test gully and is recorded by present optical unit. The time required for the detected lumen level from L_0 to 99% of L_1 is defined as the self-depuration time (T). As

an illustrative example, Fig. 1(c) depicts a typical temporal lumen variation from L_0 to L_1 with the single mixed water entry flow at the test condition of $Re_L (\alpha) = 10589 (0.56)$. As indicated by Fig. 1(c), the instant lumen value for this particular test gully increases from L_0 toward L_1 as time goes by. The temporal lumen values oscillate about L_1 reference after the time lapse exceeds T due to the presence of air bubbles in the water trap of test gully. With each tested gully of different geometries or different flow rates, the L_0 and L_1 references are accordingly varied. The temporal normalized lumen variation in terms of L/L_1 is adopted to quantitatively characterize the self-depuration performance of a gully. To clarify the air-water entry conditions, the void fractions for present mixed-water flows are detected with the results presented in Figs. 1(d) and 1(e). As the water flow rate increases, the void fraction keeps reducing, Figs. 1(d) and 1(e). Due to the differential entry angles for A, B entry pipes, the void fractions detected from entry A are consistently higher than the B-entry counterparts for both single- and twin-entry flows.

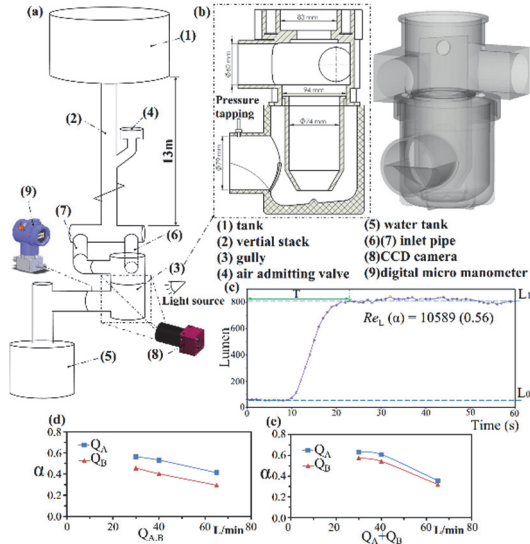


Fig. 1 (a) experimental test facilities (b) test gully (c) typical temporal lumen variation from L_0 to L_1 with single mixed water entry flow at test condition of $Re_L(\alpha) = 10589 (0.56)$; variations of void fraction against entry flow rate with (d) single (e) twin flow entry.

2.2 Numerical method

Present simulations for determining the fluid velocities and pressures are based on Navier-Stokes equations using FLOW-3D commercial code. By assuming water as incompressible fluid with unchanged viscosity, the governing flow equations for Newtonian fluid are expressed as follows:

Continuity equation:

$$\frac{\partial u}{\partial x} + \frac{\partial v}{\partial y} + \frac{\partial w}{\partial z} = 0 \quad (1)$$

Momentum equations

$$\begin{aligned} \frac{\partial u}{\partial t} + \frac{1}{V_F} \left\{ uA_x \frac{\partial u}{\partial x} + vA_y \frac{\partial u}{\partial y} + wA_z \frac{\partial u}{\partial z} \right\} \\ = -\frac{1}{\rho} \frac{\partial P}{\partial x} + G_x + f_x - b_x - \frac{R_{SOR}}{\rho V_F} (u - u_w - \delta u_s) \\ \frac{\partial v}{\partial t} + \frac{1}{V_F} \left\{ uA_x \frac{\partial v}{\partial x} + vA_y \frac{\partial v}{\partial y} + wA_z \frac{\partial v}{\partial z} \right\} \\ = -\frac{1}{\rho} \frac{\partial P}{\partial y} + G_y + f_y - b_y - \frac{R_{SOR}}{\rho V_F} (v - v_w - \delta v_s) \\ \frac{\partial w}{\partial t} + \frac{1}{V_F} \left\{ uA_x \frac{\partial w}{\partial x} + vA_y \frac{\partial w}{\partial y} + wA_z \frac{\partial w}{\partial z} \right\} \\ = -\frac{1}{\rho} \frac{\partial P}{\partial z} + G_z + f_z - b_z - \frac{R_{SOR}}{\rho V_F} (w - w_w - \delta w_s) \end{aligned} \quad (2)$$

where V_F is the fractional flow volume treated as a mass source. A_x , A_y and A_z are the fractional flow areas in x , y and z directions, respectively. In equations (1) and (2), u , v , w refer to the velocity components in x , y , z coordinate directions; P refers to static pressure, while ρ and ν refer to the density and kinematic viscosity coefficients of the fluids respectively. G_x , G_y , G_z refer to the acceleration rates of fluid particles. f_x , f_y , f_z are the viscous accelerations terms; whereas b_x , b_y , b_z refer to the flow losses in porous media or across porous baffle plates. The final terms of equation (2) account for the injection of mass at a source represented by a geometry component. u_w , v_w , w_w refer to the fluid velocities of the source components, which will generally be non-zero for a mass source at a general moving object. u_s , v_s , w_s are the fluid velocity vectors at the surface of the source relative to the source itself. With present numerical treatments,

the fluid properties are fixed at the pre-defined values.

Since the velocity-pressure form of the governing equations (1) and (2) is used based on the finite difference method to solve the transient air-water mixed flows at the single entry flow conditions. To solve the complex interfacial flow structures for such multi-entry gully flows, the present numerical scheme uses a Renormalization Group (RNG) k- ϵ model to solve the complex flow phenomena. The method was proposed by Yakhot and Orzag [17] for the incompressible flows (water) can be derived from the Eqs. (3) and (4) as follows:

$$\begin{aligned} \frac{\partial(\rho k)}{\partial t} + \frac{\partial \rho u k}{\partial x} + \frac{\partial \rho v k}{\partial y} + \frac{\partial \rho w k}{\partial z} \\ = \left(\mu + \frac{\mu_t}{\sigma_k} \right) \left(\frac{\partial^2 k}{\partial x^2} + \frac{\partial^2 k}{\partial y^2} + \frac{\partial^2 k}{\partial z^2} \right) + P_k - \rho \epsilon \end{aligned} \quad (3)$$

$$\begin{aligned} \frac{\partial(\rho \epsilon)}{\partial t} + \frac{\partial \rho u \epsilon}{\partial x} + \frac{\partial \rho v \epsilon}{\partial y} + \frac{\partial \rho w \epsilon}{\partial z} \\ = \left(\mu + \frac{\mu_t}{\sigma_\epsilon} \right) \left(\frac{\partial^2 \epsilon}{\partial x^2} + \frac{\partial^2 \epsilon}{\partial y^2} + \frac{\partial^2 \epsilon}{\partial z^2} \right) + c_{1\epsilon} \frac{\epsilon}{k} P_k - c_{2\epsilon} \rho \frac{\epsilon^2}{k} \end{aligned} \quad (4)$$

Where

$$c_{2\epsilon}^* = c_{2\epsilon} + \frac{C_\mu \eta^3 (1 - \eta / \eta_0)}{1 + \beta \eta^3}, \quad \eta = S k / \epsilon, \quad S = \sqrt{2 S_{ij} S_{ij}}$$

The related coefficients as

$$c_{1\epsilon} = 0.0845, \sigma_k = 0.7194, \sigma_\epsilon = 0.7194,$$

$$C_{\epsilon 1} = 1.42, C_{\epsilon 2} = 1.68, \eta_0 = 4.38, \beta = 0.012$$

The geometry and boundary conditions for present simulation have

been previously reported [15]. For completeness, a brief description for the boundary conditions and the simulation geometry of the test gully are provided. The geometrical scaling factor for the simulated and tested gully, as shown by Fig. 1(b), is 1:1. Thus the simulated and tested gullies have identical size and weight. Present numerical results are obtained using the fine grid cells (625,600) to attack the unsteady flow phenomena. The non-uniform mesh system is deployed with the refined grids over the regions subject to large gradient components. In this respect, the finest grid is less than 1mm for present grid system. With boundary conditions, all the solid surfaces are exceptionally subject to no-slip conditions; while the boundary conditions at the air-water interfaces have to be calculated. The upstream flow velocity (entry flow velocity) is mapping with the typical turbulent pipe flow profile with the mean-flow rate controlled at the predefined entry volume flow rate. As the outflow boundary condition is relevant to the investigation for the wave interactions with structures, the imaginative mathematical continuation for the air-water flow extends further downstream the exit port of the computational domain. This treatment is the so-called Sommerfeld radiation boundary condition; which features a simple mathematical

continuation having the form of outgoing waves:

$$\frac{\partial \phi}{\partial t} + c \frac{\partial \phi}{\partial x} = 0 \quad (5)$$

where ϕ is any quantity. With present model, ϕ refers to velocity u and positive x is directed out of the boundary and c is the local phase speed of the assumed wavy flow. Within the framework of equation (5), the mixed water flow consists of wavelike disturbances that are propagating toward the boundary. Any flow quantity ϕ at the interfacial boundary will translate across the boundary with speed c . The numerical stability conditions are satisfied by using the conservative form of the momentum equations in the discretized form as expressed by Flow-3D user manual. The time-step size used of the model is not a constant in which an optimal time step was calculated automatically based on the numerical discretizations.

Experimental uncertainties for flow rate measurements, static airflow pressures and self-depuration time are estimated according to [16]. The sources of uncertainties for these measurements are mainly attributed from the precision errors of the instrumentations. With the

volume water flow rate, static pressure and lumen in the respective ranges of 20~65 L/min, 0~ -170 Pa and 35~950 Lumen, the maximum experimental uncertainties for Re_L , static airflow pressure and self-depuration time are estimated 3.8%, 1.2% and 2.3% respectively. Regarding the validation for the aforementioned numerical results, Fig. 2 compares the calculated and measured static pressures at the flow exit with single entry flow at $Q_A=65\text{L/min}$. Three spots over the flow exit plane at the angular locations of 165° , 180° (top) and 195° are selected to collect the numerical airflow pressures. After charging the mixed water flow into the test gully at the single entry condition with $Q_A=65\text{L/min}$, the airflow pressure start decreasing with temporal oscillations along the time-mean pressure descending trend due to the agitating air bubbles within in the discharged mixed water, Fig. 2. However, the favorable agreements between the measured and calculated temporal pressure variations with the maximum discrepancy of $\pm 30\%$ are found with the transient period so that the transient results with single flow entry approximated from the numerical scheme are further analyzed.

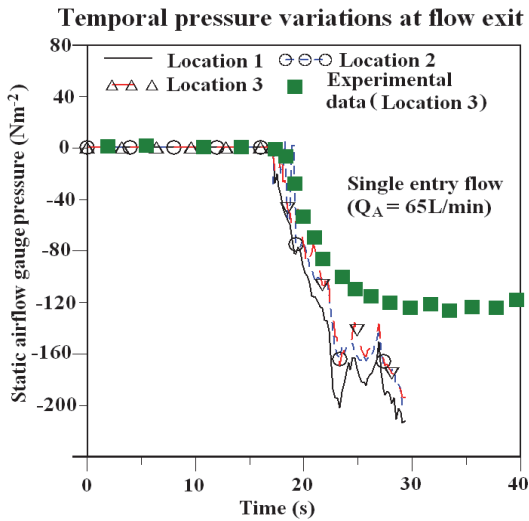


Fig. 2 Comparisons of calculated and experimental static pressures at the flow exit with single entry flow at $Q_A=65\text{L/min}$.

3. Results and discussion

3.1 Transient numerical flow results

Due to the complex interfacial flow structures for such multi-entry gully flows, the present numerical scheme is only capable of solving the transient air-water mixed flows at the single entry flow conditions. A set of selected numerical flow results with single entry mixed water flow is presented to provide the detailed insights of the transient flow phenomena emerged in present test gully. With this set of numerical flow results, the initial condition of the flow inlet for the mixed water flow entering the gully is assumed to have a constant volumetric water flow rate in a horizontal tube. The total computational domain is restricted within the multi-joint gully. The void air pressure in the gully is assumed at 1 atm ($P_a=$

$1.013 \times 10^5 \text{ N/m}^2$). All the computations have been carried out on a quad-core CPU personal computer with 4 GB RAM. The computation of CPU time is approximately evaluated 25 hrs for the complete simulation of one case.

It has shown by Fig. 2 that the present scheme used one grid size to produce the acceptable results compared to the experiments data. The Flow-3D software uses high fidelity fluid dynamics, and is applied to the fields of manufacturing and science. The theoretical foundations of Flow-3D include mass conservation equation and momentum equation. Thus, it can be applied to the majority of fluid movements of all types. The grid size used in the present model is good enough as recommendation in the Flow-3D user manual.

Figure 3 depicts the 3D transient flow pattern obtained with single entry flow of $Q_A=500 \text{ cm}^3/\text{s}$ at the selected instants of $t=1, 10, 50$ and 100 s . Initially, the agitated water flows with wavy interfacial surfaces prevail over the free surface of the mixed-water flow at $t = 1\text{ s}$. The water flow through present gully soon proceeds smoothly during this transient process. There is no sensible hydraulic jump developed in the upstream of the gully outlet for this test case. Free wavy surfaces constantly develop over the water plenum of present gully, indicating the complex

interfacial interactions between these multiple entrances which provide the airflow pathways into the gully.

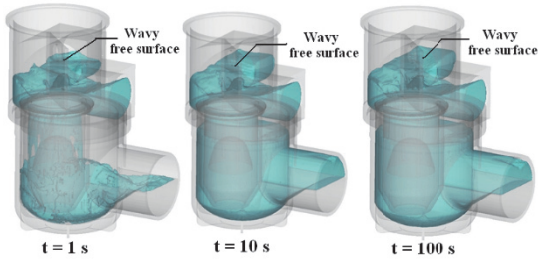


Fig. 3 3D flow patterns at various times.

Figure 4 depicts the instantaneous velocity magnitude and vectors of water flow at different time lapses during the transient process. Following the sequential flow snapshots collected in Fig. 4, the large air plenum entrained in the core of the central chamber in present gully tends to break-up, forming the disperse small-scale air bubbles in the water stream. Two swirls developed at the left and right bottoms of this gully. With the wavy free surface over the central plenum core of present gully, the air-flow is entrained from the top and side entries of present gully. A choked air bubble is formed as the water stream fills the entire flow exit as indicated by Fig. 4 at $t = 50$ and 100 s.

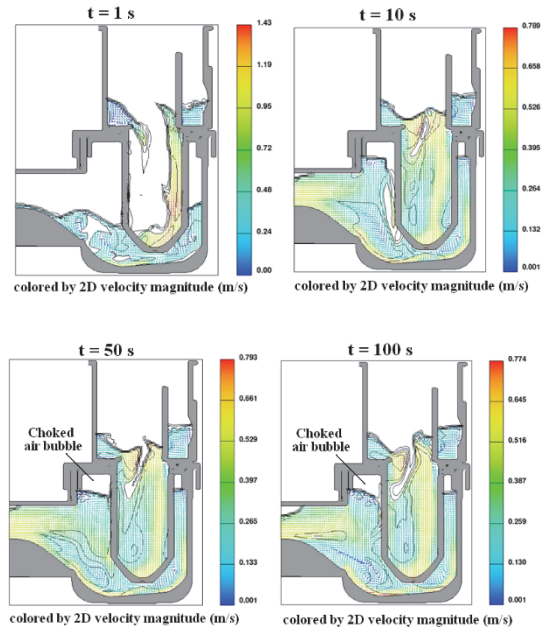


Fig. 4 Velocity magnitude and vectors at the middle plane of $y=0$.

Prior to the quasi-steady condition, the complex water streams through present gully as shown by Figs. 3-4 are motivated by local pressure gradients through the transient process. The transient pressure variations of water flow through present gully are collected in Fig. 5 which exhibits the process for building the static pressures in the gully to motivate the entry mixed water toward the flow exit. Initially, the low pressure mixed-water flow enters the gully with highly unstable oscillating interfacial boundaries over the entire volume of present gully. With 10 seconds lapse, the static pressure soon builds up with low pressure region emerged at the flow exit. Cross examining the fluid velocity contours depicted by Fig. 4, this low pressure flow region above the

exit bump shown in Fig. 5 corresponds to the high fluid velocity region in Fig. 4. The accelerated fluid flow through the streamlined convergent exit converts the pressure potential to the flow momentum, generating the low pressure region at the flow exit of pressure gully. Due to the reduced static pressures at the flow exit, the fluency of the mixed-water flow through present gully are considerably improved.

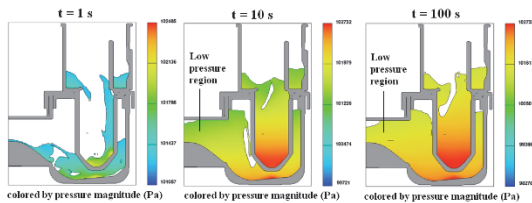


Fig. 5 Pressure contour (Pa) at the middle plane of $y=0$.

3.2 Experimental test results

Having revealed the basic air-water two-phase flow phenomena developed in present test gully with single entry flow by Figs. 3-5, the experimental results probe into the flow conditions with twin flow entrances. Particular attentions are addressed for the self-depuration performances detected by present newly devised optical method and the air-water flows imaged at the twin-entry flow conditions.

The sequential flow snapshots collected at $t=1, 10, 50$ and 100 s at $Q_A=30$ L/min, $Q_B=30$ L/min with single-entry flows and $Q_A=Q_B=15$ L/min and $Q_A=Q_B=30$ L/min with twin-entry flows

are collected in Fig. 6.

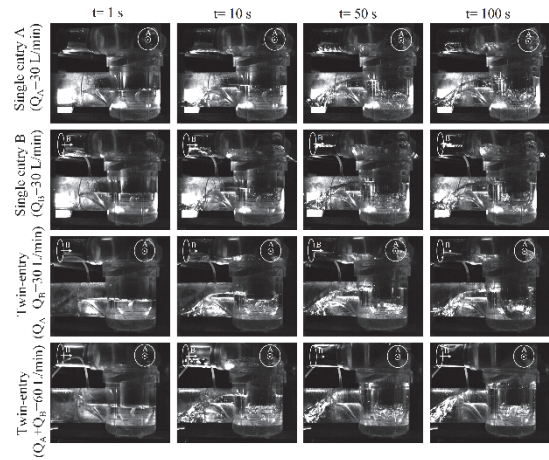


Fig. 6 Sequential flow snapshots collected at $t=1, 10, 50$ and 100 s at $Q_A=30$ L/min, $Q_B=30$ L/min with single-entry flows and $Q_A=Q_B=15$ L/min and $Q_A=Q_B=30$ L/min with twin-entry flows.

Irrespective to the single or twin entry flow conditions, the air bubbles taking the typical bubbly flow structures emerge at the bottom of the central liquid pool of present gully and at the location downstream the streamlined bump, Fig. 6. With the stratified mixed water entering the gully core from the horizontal inlet pipe, the highly unstable wavy-like free surface prevails over the annular flow surrounding the central gully core. Over the top surface of such unstable wavy free-surface, the agitating water stream entrains airflow into downward the core chamber of present gully. At the bottom of central core, the impinging mixed-water stream undergoes considerable pressure variations upon impingement, leading to considerable pressure relaxations to release the entrain air from the water

stream. A cluster of small-scale air bubbles are accumulated/trapped underneath the central plenum with limited and dispersed air bubbles drifting in the downstream water stream toward the streamlined bump at the exit of present gully. With the twin entry flow condition of $Q_A=Q_B=30\text{L}/\text{min}$, the maximum discharged flow rate about $60\sim 65\text{L}/\text{min}$ is approaching. With the discharged flow rate approaching the maximum capacity, the water flow tends to fill the entire throat of the converging flow exit. Such criterion for setting the maximum discharge capacity of present gully is clearly demonstrated by depicting the flow images detected at the quasi-steady states with single and twin-entry flows, Fig. 7.

Figure 7 depicts the flow images detected at $Q = 30, 40$ and $65\text{L}/\text{min}$ with single and twin entry flows. Even with the two orthogonal flow entries, namely entry A and entry B as indicated in Fig. 7, the air-water flow structures developed in present test gully follow the similar pattern. In this respect, the air-bubble cluster accumulated underneath the central core plenum with wavy-like free surfaces emerging at the top end of the central plenum and downstream the streamlined exit bump, Fig. 7. With either single or twin entry flows, the water flow fills fully the throat of the convergent flow exit at the maximum discharge capacity of

$65\text{L}/\text{min}$. Further performance improvements are thus directed toward the stabilizing air-bubble agitation /segregation underneath the central plenum of present gully and/or the extending flow rate through the throat of the convergent flow exit.

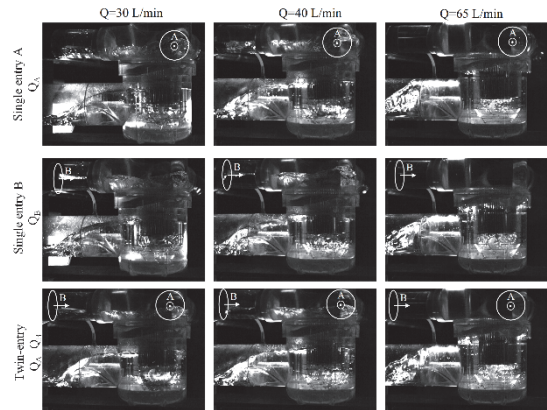


Fig. 7 Flow images detected at $Q= 30, 40$ and $65\text{L}/\text{min}$ with single and twin entry flows.

With applications to the drainage system of a building, it is also important to minimize the unfavorable impacts on the discharged air-water flow downstream the gully. Thus the temporal variations of airflow pressure are detected at various mixed water flow rates. For present test gully, the installation of streamlined bump downstream the flow exit considerably stabilizes the air-water flows through the gully. With the total flow rate of mixed water less than the maximum discharging capacity, the temporal variations of airflow pressure downstream the flow exit of present test gully are extremely stable, which are exemplified by Fig. 8(a) in which the instant airflow pressures

recorded through the transient process after the single discharges of $Q_A=40\text{L/min}$ or $Q_B=40\text{L/min}$ and the twin-discharge of $Q_A=20\text{ L/min}$ and $Q_B=20\text{L/min}$ are compared. The stable airflow pressures at the atmospheric level are confirmed. When the single or twin flow rates reach the maximum discharge capacity of present test gully of 65 L/min , the airflow pressures become sub-atmospheric. In this regard, the airflow pressures downstream the test gully at the twin-entry flow condition of $Q_A=Q_B=32.5\text{L/min}$ are subject to the less impact, which is followed by the single entry flow from entry B at $Q_B=65\text{L/min}$ and the most severe impact at the single entry flow from entry A at $Q_A=65\text{L/min}$, Fig. 8(b). With the exit throat being fully filled by the mixed water at the maximum discharging flow rate as depicted by Fig. 7, the sub-atmospheric levels of airflow pressure are closed relevant to the entrain airflow from the flow entry. With twin-entry flows, the patterns of the interfacial flow structures in the horizontal entry pipe remain as the stratified wavy flows, enabling the airflow entrainment into the entry mixed-water flow. However, with the single entry flow at the maximum flow rate of $Q_A=65\text{L/min}$ or $Q_B=65\text{L/min}$, the entire inlet pipe is filled with water flow so that the air entrainment from the incoming entry mixed water stream is considerably

moderated. The differential sub-atmospheric levels between the single entry flow conditions of $Q_A=65\text{L/min}$ or $Q_B=65\text{L/min}$ are attributed to the discharging capacity of the air bubbles from the bubble cluster accumulated underneath the central core of present gully. When the entry flow pipe (entry B) is in parallel with the exit pipe of present gully, the better air-bubble discharge from the bubble cluster underneath the central plenum can be achieved. With the single flow entry from pipe A which is orthogonal to the discharge pipe of present gully, the strength of swirl developed underneath the central plenum seems to be weakened from the entry B scenarios. Further swirling enhancement underneath the central plenum for the hydrodynamic performances of present test gully is worthy of future investigations.

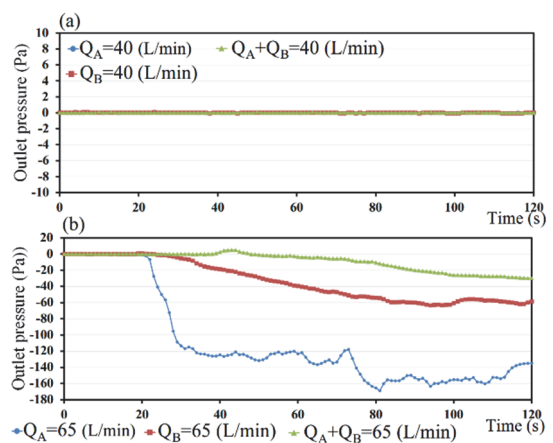


Fig. 8 Temporal variations of airflow pressure with single and twin entry flows at

(a) $Q_A=40\text{ L/min}$, $Q_B=40\text{ L/min}$ and twin-discharge of $Q_A=Q_B=20\text{ L/min}$ (b) $Q_A=65\text{ L/min}$, $Q_B=65\text{ L/min}$ and twin-discharge of $Q_A=Q_B=32.5\text{ L/min}$.

Another aspect which is worthy of investigation is the capability of self-depuration for a multi-entry gully. The test results collected from the optical measurement method illustrated in Fig. 1 for present test gully are shown by Fig. 9 with (a) single A entry of $Q_A = 20, 30, 40, 65$ L/min (b) single B entry of $Q_B = 20, 30, 40, 65$ L/min (c) twin A and B entry with $Q_A = Q_B$ of $Q_A + Q_B = 20, 30, 40, 65$ L/min. As indicated by each temporal L/L_1 variations shown in Fig. 9, the self-depuration performance of present test gully is characterized as a “waiting period” followed by the exponential-like curve at each test condition. At low flow rate of $Q_A = Q_B = (Q_A + Q_B) = 20$ L/min, the L/L_1 curves shown in the respective Figs. 9(a), 9(b) and 9(c) undergo a substantial period of waiting period during which the L/L_1 ratios remain at about zero. Thus the replenishment of fresh mixed water during the waiting period is considerably limited. However, by way of momentum enrichment for the entry mixed water flow, the waiting period is consistently reduced as the discharging flow rate through the test gully increases, Figs. 9(a)-9(c). After the waiting period, the following L/L_1 ratios raise rapidly with diminished L/L_1 agitations, Figs. 9(a)-9(c). Within this particular period, the cluster of air bubbles underneath the central plenum is not yet developed so that the transparency of the

scanned test gully can be rapidly improved, reflecting the effective/efficient replenishment of fresh mixed water with lesser degrees of form/frictional drags induced by the air-bubbles. Having transited through the period of rapid replenishment, the L/L_1 ratios are steadily increased at the moderate rate with the most noticeable L/L_1 agitations in this final stage. Clearly, the agitating L/L_1 ratios at the final stage are caused by the drifting air bubbles in the water stream which prohibit the effective/efficient replenishment of fresh mixed water by weakening the through flow momentum due to the enhanced form/frictional drags at the interfacial boundaries of these agitating air bubbles. The typical distributing pattern of L/L_1 , which exhibits consistently for the data trends collected in Fig. 9, shows a waiting period during which the air-water flow in the gully is under development with insufficient discharging momentum for self-depuration. To overcome the partial blockage of air bubble(s) in the gully and reinforce the discharging momentum during the waiting period, the adding swirls by fitting skewed surface ribs inside the drum of a gully is worth of further investigations for design improvements of a gully. Nevertheless, as described previously, the self-depuration duration (T) is defined at $L/L_1 = 0.99$. The various T

values obtained from the self-depuration tests are collected in Table 1.

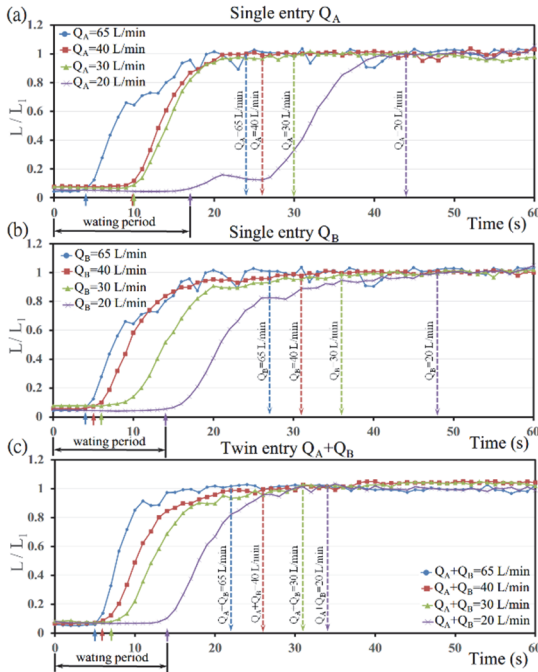


Fig. 9 Temporal variations of L/L_1 with (a) single A entry of $Q_A=20, 30, 40, 65$ L/min

(b) single B entry of $Q_B=20, 30, 40, 65$ L/min (c) twin A and B entry with

$$Q_A = Q_B \text{ of } Q_A+Q_B=20, 30, 40, 65 \text{ L/min.}$$

Table 1 Self-depuration durations (T) at single and twin entry conditions.

Q (L/min)	T (s)		
	Single entry (A)	Single entry (B)	Twin entry (A+B)
65	24	27	22
40	26	31	26
30	30	36	31
20	44	48	34

The variations of self-depuration duration (T) against the total discharge flow rate (Q) with single and twin flow entry conditions are compared in Fig. 10. At each flow entry condition, the self-depuration durations keep reducing as Q

increases, Fig. 10. At a fixed Q, the order of the self-depuration durations (T) generally follow the order of $T_A > T_B > T_{A+B}$ as compared by Fig. 10. Following the consistent Q-driven T varying trends depicted in Fig. 10, three sets of empirical T correlations are devised as equations (4)-(6) as the design aid for approximating the self-depuration duration using present test gully.

$$T_A = 89.6 - 16.43 \ln Q \quad \text{Single A entry} \quad (4)$$

$$T_B = 98.02 - 17.54 \ln Q \quad \text{Single B entry} \quad (5)$$

$$T_{A+B} = 66 - 10.59 \ln Q \quad \text{Twin A+B entry} \quad (6)$$

Justified by the consistent test results depicted in Figs. 9-10, the present newly devised optical measuring method for determining the self-depuration duration of a test gully involving complex interfacial flow structures is favorably demonstrated; which can be adopted to quantitatively assess the self-depuration duration of a gully.

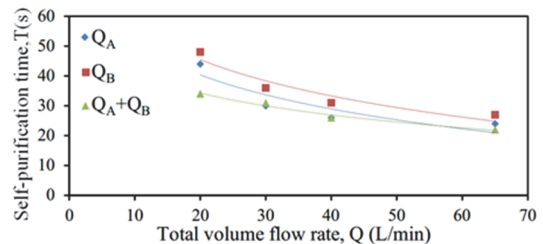


Fig. 10 Variations of self-depuration duration (T) against total discharge flow rate (Q) with single and twin flow entry conditions.

3. Conclusions

This work adopts the numerical and experimental methods to examine the hydrodynamic performances of the multi-entry gully with drainage applications for a building. The following salient remarks emerge from this study.

1. The presence of a streamlined bump downstream the flow exit of the multi-entry gully assists to stabilize the upstream air-water flow by generating the low pressure region at the convergent throat of the flow exit.
2. The entrained airflow transits into air-bubble cluster underneath the central plenum of present test gully after the impingement of the downward mixed-water stream. These agitated small-scale air bubbles increase the form/frictional drags over the interfacial boundaries to weaken the exit flow momentum for prohibiting the effective/efficient replenishment of fresh mixed water.
3. The maximum discharge capacity of present test gully at either single or twin entry conditions are limited by the choked flow at the convergent throat downstream the flow exit.
4. A newly devised optical measuring method for quantitatively determining the self-depuration duration of a gully involving complex interfacial flow structures is

developed. The typical three-stage temporal L/L_1 variations constituted by the “waiting period”, “rapid increase period” and “steadily moderate increase” period is disclosed for present test gully.

5. The self-depuration period at either single or twin entry condition consistently decreases as Q increases. Three set of empirical T correlations are devised to assist the relevant building applications.

References

- [1] J.A., Swaffield, D.P. Campbell, (1992) Air pressure transient propagation in building drainage vent systems, an application of unsteady flow analysis, *Building and Environment* 27: 357-365.
- [2] J.A. Swaffield, D.P. Campbell, (1995) The simulation of air pressure propagation in building drainage and vent system, *Building and Environment* 30: 115-127.
- [3] S.W. Chang, C.-M. Hsieh, C. Y. Lin, H.-F. Liou, (2012) Air-water drainage flow through finned bend, *Journal of Asian Architecture and Building Engineering* 11: 177-184.
- [4] J.A. Swaffield, L.B. Jack, D.P. Campbell, (2004) Control and suppression of air pressure transients in building drainage and vent systems,

- Building and Environment 39: 783-794.
- [5] S.W. Chang, D.C. Lo, (2009) Advances in multiphase flow and heat transfer 2: 176-215. Chapter 6 Air-Water Two-Phase Flows with Applications to Drainage System, Bentham Science Publishers Ltd.
- [7] 張始偉；楊春陵；劉新豐，浴室排水匯流裝置結構，中華民國專利新型第 M338857 號 (2008-August, 2018-January).
- [8] 張始偉；楊春陵；劉新豐，浴室排水匯流裝置結構(二)，中華民國專利新型第 M345088 號 (2008-November, 2018-June).
- [9] 劉新豐；張始偉，浴室排水匯流裝置結構(三)，中華民國專利新型第 M362254 號
- [10] 張始偉；劉新豐，浴室排水匯流裝置結構，中華人民共和國實用新型專利證書 證書號第 1392955 號 (2009-June, 2019-June).
- [11] 張始偉；劉新豐，浴室排水匯流裝置結構，中華人民共和國實用新型專利證書 證書號第 2222003 號 (2011-September, 2021- September).
- [12] 張始偉；劉新豐，浴室排水匯流裝置結構改良，中華民國專利新型第 M434797 號 (2012-August, 2021-September).
- [13] EN 1253-2 Gullies for buildings – Part 2: Test methods, European standard, December 2003.
- [14] CNS 14431 Q3001 油脂截留器性能試驗法，中華民國國家標準，May 2000.
- [15] D.-C. Lo, S-F. Liou, S.W. Chang, Hydrodynamic characteristics of confluent unit device for drainage system, 2012 SPSEA Proceedings, pp. 271-280, 2nd International Symposium on Plumbing System in East Asia, 3rd November, 2012, National Taiwan University of Science and Technology, Taipei, Taiwan.
- [16] Editorial Board of ASME Journal of Heat Transfer, (1993) Journal of Heat Transfer Policy on Reporting Uncertainties in Experimental Measurements and Results, ASME J. Heat Transfer 115: 5-6.
- [17] V. Yakhot, S. A. Orszag, (1986) Renormalization group analysis of turbulence, I: basic theory, Journal of Scientific Computing 1: 3-51.

全球暖化對臺灣未來水資源之母嚮評估

張昭銘* 國立高雄海洋科技大學海產資訊科技系
蔡雅琴 國立高雄海洋科技大學海產資訊科技系

*通訊作者 Email: cjming@mail.nkmu.edu.tw; Tel: +886-7-8100888 ext. 5307
(2014年3月4日收稿; 2014年4月10日定稿)

摘要

本文運用聯合國跨政府氣候變遷小組(IPCC)所執行未來百年之氣候預報實驗, 評估未來全球暖化對臺灣地區水資源之可能影響。分析結果顯示, 臺灣夏季溫度於未來百年, 將呈現100%機率之偏暖趨勢, 偏暖強度與未來全球溫室氣體含量成線性對應關係, 較高溫室氣體含量對應較高暖化程度。在夏季降雨方面, 臺灣地區降雨約有2/3 機率為偏多趨勢, 但與溫室氣體含量無線性對應關係。臺灣夏季降雨偏多主要來自東南側洋面之颱風活動增強, 預期於2100年侵臺颱風將倍增, 帶來更多颱風雨。颱風所帶來豪大雨, 不易為臺灣現行三大水資源系統(水庫、河川水、地下水)所用, 且會危及其執行效率, 因此建議強化建置家庭式與社區性的水資源小系統, 以達充份運用水資源之效。

關鍵字: 水資源, 全球暖化, 颱風雨

Abstract

The possible impacts of global warming on future water resources in Taiwan are surveyed from the climate prediction experiments conducted by the Intergovernmental Panel on Climate Change (IPCC). Analysis results show that future summer temperature in Taiwan has a 100% chance of significant warming. The warming intensity is proportional to the concentrations of green-house gases. The future summer rainfall tends to have a 2/3 chance of significant increase. The increasing intensity is independent of the concentrations of green-house gases. The major processes of increasing summer rainfall appear to be related to more typhoon activity over the oceans to the southeast of Taiwan. Severe typhoon rainfall cannot be efficiently used by the current major water resource systems, including reservoirs, rivers, and underground water. On the other hand, it may deteriorate the present water resource

operations. It suggests to broadly establish individual small water resource systems in family and community to increase the total efficiency of water resource operation.

Keywords: Water resource, Global warming, Typhoon rainfall

一、前言

國際間當今最熱門環境議題之一，為全球暖化現象方興未艾，聯合國所屬的跨政府氣候變遷小組(Intergovernmental Panel on Climate Change, IPCC)於2007之第四份評估報告指出，全球暖化之急速增速現象，百分之九十可能性為人為因素造成(IPCC, 2007)，而於2013年之第五份評估報告，更加確認此結果，指出高達百分之九十五可能性為人為造成(IPCC, 2013)。全球暖化所造成之衝擊是全面性，氣溫上升維持長期偏暖狀態，大氣與海溫上升，造成水氣蒸發量增加，偏暖之空氣又可容納更多水氣，在大氣水氣偏多背景之下，降雨量預期趨於偏多，Liu et al. 2009)分析1979-2007年降雨觀測資料指出，當全球平均溫度上升1度，全球降雨強度將增23%，在溫度與降雨產生連動變化之下，各地之氣候狀態與生態環境將產生明顯變化。

全球暖化對區域氣候之影響，因地而異，降雨之變化亦是如此。當氣溫升高之際，各地增溫幅度有所不同，一般而言，陸地高於海洋，北半球高

於南半球，極區高於熱帶(許, 2009)，溫差造成熱源中心之異動，伴隨而來之高壓與低壓距平，帶動各地氣流變化，水氣傳送隨之變化，進而影響各地降雨型態與強度。過去研究指出，臺灣氣候明顯受到大尺度環流變化之影響，包括氣溫與降雨(Chen et al. 2005; Chen et al. 2008a; Chen et al. 2010ab; Chen and Chen 2011)。在溫度方面，臺灣過去百年呈現長期增溫趨勢，其增溫幅度約為全球平均值(0.60C/100年)之1-2.5倍(0.6~1.40C/100年)，其中以夏季增溫最大，冬季最小(陳與汪2000)。在區域分佈方面，都會區增溫幅度約為全球平均值之2倍，人口稀少之非都會區則與全球平均值相當(Chen et al. 2008b)，此結果顯示，臺灣地區氣候明顯受到全球暖化的影響，而都會區增溫趨勢高於非都會區，其中強度差異值應與都會區人口密集所造成都市效應之額外增溫結果有關。

在降雨方面，臺灣主要雨季來自西南氣流相關之季風雨(梅雨、午後雷陣雨)與颱風雨(陳2006)。於1950-2008年之夏季中，臺灣地區之颱風降雨呈現上升趨勢(324 mm/100年)，季風雨呈現下降趨勢(-224 mm/100年)，整體而言，降雨總量為增加趨勢(100 mm/100年)，增加來源主要源自颱風雨之增加(Chen and Chen, 2011)，歸其主因則是夏季侵臺颱風呈現增加趨勢(+3.1個/100年)，相對於每年夏季2-3個侵臺颱風數目(中央氣象局, 2006)，預期2100年時，夏季侵臺颱風數會呈

現倍增現象，其衝擊當不容忽視。在全球暖化背景之下，未來氣候變遷將更形劇烈，預期颱風之強度與生命週期將更為加強(Emanuel 2005; Webster et al. 2005; Oouchi et al. 2006)，在颱風活動改變之背景之下，臺灣地區之降雨型態與水資源管理，勢必須有調適因應之預防措施。

經濟部水利署(2012)統計資料顯示，臺灣地區之平均年雨量約 2500 mm，相當 951 億噸水量，平均蒸發量為 21%，平均逕流量為 74%，地下水入滲量為 5%。逕流量中，78%直接入海，22%為地面水可供使用。地面水與地下水入滲量共計約 181 億噸，約佔總降雨量之 19%。這些水資源 20%屬生活用水，9%屬工業用水，71%屬農業用水。在水資源之使用方式，24%由水庫系統維持，56%由河川直接引水，20%為抽取地下水。為了防止地層下陷及各地重大交通工程之安全維護，地下水抽水量已從 1996 年之 30%降至 2010 年之 20%，而水庫用水則由 20%升到 24%，反應水庫功能之倚重日深。

然而如 2009 年莫拉克颱風之破紀錄降雨所引發之慘重災情，颱風強降雨易引發上游集水區之地形崩塌，大量土石下沖造成水庫淤積，一來有危水庫安全，二來降低水庫運作績效，顯現颱風等極端降雨事件，對臺灣水庫運作與水資源供應管理均會造成潛在威脅。在水資源供應穩定性的考量之下，未來全球暖化所可能引發的極端天氣對臺灣降雨量與降雨型態之影

響方式與程度為何，及其對水資源運作之可能衝擊為何，均值得進一步來探討。本文之主要目的即以未來全球暖化情境下臺灣地區降雨之可能變化為分析對象，並將其分析應用於探討臺灣未來水資源供應之可能變化，以供決策單位參卓擬定適宜之氣候變遷調適策略，期以維持臺灣水資源之安全運作管理，促進經濟發展與民生福祉。

二、研究資料與分析方法

(一) 研究資料

為了討論未來氣候變遷之可能狀態，本文運用聯合國 IPCC 所執行之氣候模式預報實驗進行分析，該模式係以 1990 年全球溫室氣體含量為基準，依據未來人口增加、能源使用、經濟活動、土地利用等不同變化情境預估做為背景，據以推估全球溫室氣體之可能變化情形，再將此情形做為環境背景，趨動海洋-大氣耦合模式進行數值預報，預測未來百年內之全球大氣與海洋之氣候變化狀態，進而分析全球暖化對各地區之衝擊情形，藉以分析未來全球暖化之下，各地之氣候變遷與環境變異之可能發展情形。

依據 IPCC(2007)所發佈之第四份年度評估報告結果，IPCC 預估未來全球暖化之情境分為三級，其 2100 年之全球溫室氣體含量分別為重度暖化之 860 ppm，命名為 A2 情境；中度暖化之 720 ppm，命名為 A1B 情境；輕度暖化之 550 ppm，命名為 B1 情境。相

較於 1990 年之 360 ppm，其增加倍率分別約為 2.5，2，1.5 倍。各情境 CO₂ 濃度之變化情形，如圖 1 所示。

本文依據 IPCC(2007)第四份評估報告所完成對 2000-2100 年之氣候變遷預測實驗進行分析，以臺灣鄰近區域之網格點區域平均值，取夏季溫度與降雨進行分析未來百年之可能氣候變化趨勢。IPCC 不同情境預報，分別由全球各主要氣象中心與研究單位執行，B1 情境共有 44 個模式預報實驗，A1B 情境共有 49 個預報實驗，A2 情境有 37 個預報實驗，個情境所選取之預報實驗如表 1 所列，並將作為本研究之分析對象。

(二) 分析方法

在本研究中，未來氣候之長期變化趨勢為分析重點，趨勢斜率之顯著程度可用 Student's *t* 方法檢驗 (Woodward and Gray, 1993; Chu and Wang, 1997)。設定某一時間序列 ($Y_t, t = 1, \dots, n$) 依簡單線性回歸計算所得之截距 (intercept) 與斜率 (slope) 為 \hat{a} and \hat{b} ，則其斜率之標準誤差 (standard error) 可估算為：

$$SE(\hat{b}) = \left[\frac{\sum_{t=1}^n (Y_t - \hat{a} - \hat{b}t)^2}{(n-2) \sum_{t=1}^n (t - \bar{t})^2} \right]^{1/2}$$

其中 t 為時間， \bar{t} 為 t 之平均值。Student's *t* 統計量計算為 $\hat{b}/SE(\hat{b})$ ，當其顯著程度達到 0.05 等級時，即視為顯著個案。

表 1: 本研究所分析之 A1B、A2、B1 情境之各個模式

A1B		A2		B1		
bccr_bcm2_0	1	bccr_bcm2_0	1	bccr_bcm2_0	1	
cccma_cgcm3_1	1	cccma_cgcm3_1	1	cccma_cgcm3_1	1	
	2		2		2	
	3		3		3	
	4		4		4	
	5		5		5	
cccma_cgcm3_1_t63	1	csiro_mk3_0	1	cccma_cgcm3_1_t63	1	
cnrm_cm3	1	csiro_mk3_5	1	cnrm_cm3	1	
csiro_mk3_0	1	gfdl_cm2_0	1	csiro_mk3_0	1	
csiro_mk3_5	1	gfdl_cm2_1	1	csiro_mk3_5	1	
gfdl_cm2_0	1	ingv_echam4	1	gfdl_cm2_0	1	
gfdl_cm2_1	1	inmcm3_0	1	gfdl_cm2_1	1	
giiss_model_e_h	1	ipsl_cm4	1	iap_fgoals1_0_g	1	
	2		1		2	
	3		2		3	
iap_fgoals1_0_g	1	miroc3_2_medres	3	inmcm3_0	1	
	2		1		ipsl_cm4	2
	3		2		miroc3_2_hires	3
ingv_echam4	1	mpi_echam5	3	miroc3_2_medres	1	
inmcm3_0	1		1		2	
ipsl_cm4	1		2		3	
miroc3_2_hires	1	mri_cgcm2_3_2a	3	miroc3_2_hires	1	
miroc3_2_medres	1		4		2	
	2		5		3	
	3	ukmo_hadcm3	1	mri_cgcm2_3_2a	1	
1	1	2				
2	2	3				
mpi_echam5	1	miub_echo_g	2	mri_cgcm2_3_2a	3	
	2		3		4	
	3		3		4	
	4		1		5	
	1		2		ukmo_hadcm3	1
mri_cgcm2_3_2a	1	ncar_ccsm3_0	3	miub_echo_g	1	
	2		4		2	
	3		5		3	
	4		1		1	
	5		2		2	
ukmo_hadcm3	1	ncar_pcm1	3	ncar_ccsm3_0	3	
miub_echo_g	1		4		5	
	2		1		6	
	3	2	7			
ncar_ccsm3_0	1	ncar_pcm1	3	ncar_ccsm3_0	9	
	2		4		1	
	3		1		2	
	4		2		3	
	5		3		4	
	6		4		1	
	7		3		2	
9	4	3				
ncar_pcm1	1	ukmo_hadgem1	1	ncar_pcm1	4	
	3		1			
	4		2			
ukmo_hadgem1	1					

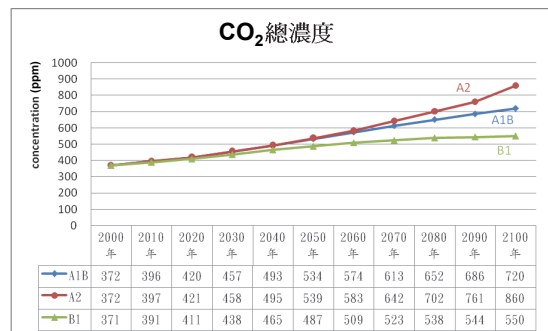


圖 1: IPCC A2, A1B, B1 情境之 CO₂ 濃度變化情形 (摘錄自 許 2009)

三、臺灣夏季溫度之變化趨勢

本文取每一個實驗預報結果，計算臺灣週邊區域 2.5° 網格點 (120°-125°E, 20°-25°N, 共計 3 x 3 = 9 網格點) 之平均值，以夏季(6-8 月)溫度之季節平均值為分析對象，計算 2000-2100 年時間序列之斜率，依此推估未來臺灣氣候之可能變化趨勢，並分析斜率之顯著程度。如表 2 所示，臺灣夏季溫度於 2000-2100 年間預測出現全面性顯著增溫現象，所有 49 個 A1B 實驗，37 個 A2 實驗，44 個 B1 實驗，均預報臺灣夏季未來將會顯著增溫。A1B 的 49 個實驗之溫度時間序列呈現如圖 2，各個實驗由於其模式氣候與預報特性不同，預報之溫度範圍自 296 K 到 303 K，約等於 23°C 到 30°C，與臺灣夏季氣溫之變化範圍相近。圖 2 各實驗雖清楚呈現明顯增溫趨勢，但其強度均有所不同，為了進一步量化未來之增溫範圍，本文計算每一個實驗之臺灣夏季溫度的百年溫度上升率，並計算所有實驗之平均值，以進行不同暖化情境之增暖程度比較。

圖 3 所示為臺灣夏季溫度百年增溫率之範圍及其平均值，B1 實驗之百年增溫範圍為 0.5875-3.7824°C，A1B 實驗之增溫範圍為 1.3005-7.3780°C，A2 增溫範圍為 1.8814-7.8051°C。B1，A1B，A2 三個實驗分別對應 550ppm、720ppm、860ppm，而其平均百年增溫率則分別是 1.8164°C、2.9873°C、3.8912°C，顯現於較高溫室氣體含量之下，增溫強度將更強，這也反應一般

觀念，較高溫室氣體含量將促成較強暖化現象，各情境實驗溫度平均值之百年時間序列如圖 4 所示，到 2100 年時，A2 之平均溫度為 303 K，A1B 約為 302.5 K，B1 約為 301.5 K，相當於 30°C，29.5°C，28.5°C，上述分析結果佐證 IPCC 所推論目前全球暖化現象之主要成因為溫室氣體之增加。

表 2：IPCC 不同暖化情境所預報臺灣夏季

(JJA)溫度(Tas)顯著偏暖(+)與顯著偏冷(-)之個案數分佈表。

溫度 (Tas)	JJA			個案數
	A1B	A2	B1	
+	49	37	44	134
-	0	0	0	0
機率	49/49 (100%)	37/37 (100%)	44/44 (100%)	

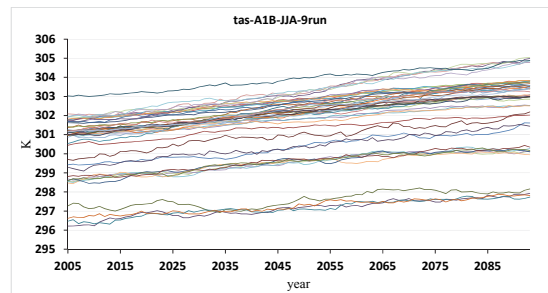


圖 2：IPCC A1B 情境所預報臺灣地區溫度呈現偏暖趨勢實驗之溫度變化趨勢圖。(單位：K)

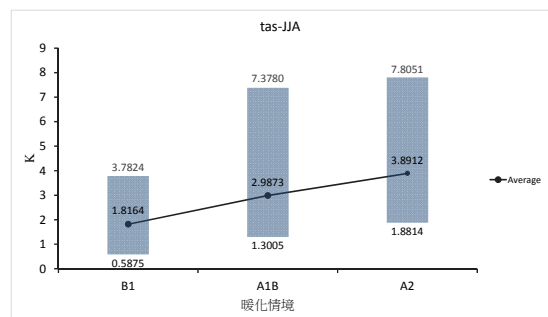


圖 3：IPCC 不同暖化情境所預報臺灣夏季溫度之百年增溫率範圍(柱狀圖)及平均值(實線)。(單位：K)

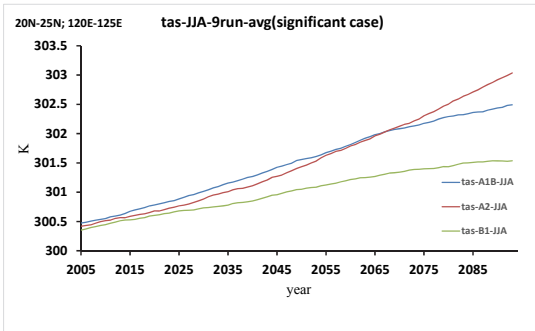


圖 4：IPCC 不同暖化情境所預報臺灣夏季溫度之所有實驗平均值的暖化趨勢圖。(單位：K)

四、臺灣夏季降雨之變化趨勢

依照前述對夏季溫度之分析方法，本文計算臺灣區域(120°-125°E, 20°-25°N) 3x3 網格點之夏季降雨平均值，計算各情境實驗降雨預報之 2000-2100 年時間序列之斜率，並依其統計顯著程度，將顯著正斜率與顯著負斜率個案分類分析，其結果如表 3 所示。於 A1B 的 49 個預報實驗中，顯著降雨偏多為 34 個，顯著降雨偏少為 8 個，A2 的 37 個預報實驗中，顯著降雨偏多為 24 個，顯著降雨偏少為 4 個，B1 的 44 個預報實驗中，顯著降雨偏多為 29 個，顯著降雨偏少為 8 個，整體而言，顯著降雨偏多個案數明顯高於顯著降雨偏少個案數，其比例於 A1B 預報實驗為 $34/49=69\%$ ，A2 預報實驗為 $24/37=64\%$ ，B1 預報實驗為 $29/44=66\%$ ，佔所有實驗約 2/3 強，呈現為主要特性。由此結果可推論，未來於 2000-2100 年間，臺灣夏季降雨主要特性為降雨偏多趨勢，其可能性高達 64-69%，約 2/3 強。

本文針對降雨之預報特性分析，將以偏多趨勢之主要特性為分析對象，圖 5 所示為 A1B 實驗降雨顯著偏多的

34 個預報實驗之 2000-2100 年時間序列，整體而言，其增加趨勢雖不若夏季溫度明顯，但仍為緩慢增加現象。各實驗降雨偏多趨勢之範圍及平均值如圖 6 所示，B1 實驗之百年增加趨勢為 0.0023-1.6311mm，A1B 實驗為 0.0134-3.7022mm，A2 實驗為 0.0163-1.4287mm，A1B 實驗之預報變化範圍最大，A2 最小。就平均值而言，B1、A1B、A2 之百年降雨增加趨勢分別為 0.2972mm、0.5453mm、0.2048mm，以 A1B 最高，B1 其次，A2 最小。夏季溫度之增溫趨勢與溫室氣體含量呈現線性對比關係，高溫對應較高溫室氣體含量，但降雨與溫室氣體含量則無此線性對應關係，降雨係受環流變化與水氣傳送影響，二者均會對應熱源變化而變異，而熱源的分佈對比，方是決定環流變化的機制，總熱源並非決定因素。溫室氣體增多主要反應於總熱源的增加，而非熱源分佈的差異，因此降雨與溫室氣體含量未能呈現線性對應關係。

表 3：IPCC 不同暖化情境所預報臺灣夏季

(JJA)降雨(Pr)顯著偏多(+)與顯著偏少(-)之個案數分佈表。

降雨 (Pr)	JJA			個案數
	A1B	A2	B1	
+	34	24	29	89
-	8	4	8	20
機率	34/49 (69%)	24/37 (65%)	29/44 (66%)	

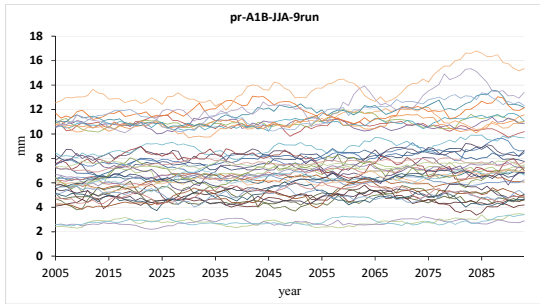


圖 5：IPCC A1B 情境呈現臺灣夏季降雨增多趨勢之時間序列圖。(單位：mm)

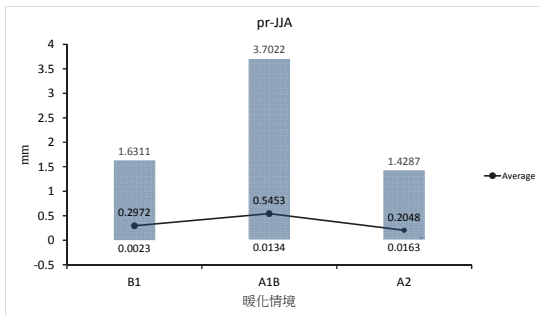


圖 6：IPCC 不同暖化情境所預報臺灣夏季降雨之百年增加率之範圍(柱狀圖)及平均值(實線)。(單位：mm)

五、夏季降雨之時空間分佈特性

IPCC 實驗預報有超過 2/3 機率顯示臺灣夏季降雨為偏多趨勢，由於臺灣夏季降雨主要來源分為季風雨與颱風雨兩種，其佔總降雨之百分比分別為 47.5%與 52.5%(Chen et al. 2010 b)，而季風雨包含西南氣流降雨與午後雷陣雨，天氣系統多由臺灣西南側之南中國海往臺灣移入。另一方面，颱風雨則由颱風侵臺時所引發之降雨，颱風生成位置主要位於熱帶西太平洋與菲律賓東側海面，中央氣象局(2006)將颱風侵臺路徑分為 9 類(圖 7)，其中第 1 類到第 6 類的路徑均是由臺灣東南側

海面往臺灣移入，其所佔比例約為全部侵臺颱風之 80% (中央氣象局 2006)，由此可見颱風侵臺之主要區域為自東南側海域移入臺灣，與季風雨發生於西南側海域之空間分佈有所不同，此空間分佈差異可供進一步研究未來降雨偏多之主要時空間分佈特性，藉此分析對應降雨之主要類型。

為了分析臺灣未來降雨偏多之主要降雨類型，本文選取 A1B 實驗具有降雨顯著偏多趨勢的 34 個實驗，取其 2000-2100 年夏季平均降雨，計算 34 個實驗之平均值，再運用 9 年滑動平均值，濾去年際變化分量，以緩慢變化之年代際分量來分析變化趨勢。為了同步顯現降雨之時空間分佈特性，本文選取 90°-180°E，EQ-50°N 範圍之降雨量，執行經驗正交函數分析，其結果顯現於圖 8。第一模態變異量佔全部變異量之 85%，可反應其主要變化特性，故可用來解釋未來變化趨勢之主要特性。第一模態之時間序列(圖 8a)呈現一條遞增趨勢，反應未來變化趨勢幾近線性狀態。而其對應空間分佈型態(圖 8b)幾乎全部為正值，反應未來於溫室氣體增多背景之下，亞洲-太平洋區之夏季降雨將因高溫而傾向增多。在空間型態中，主要增加區域為熱帶西太平洋-中太平洋地區(140°-180°E)，此區域約為所謂的暖池區，另一顯著地區，位於臺灣東南側的熱帶洋面(120°-140°E, 10°-20°N)，此區域為主要颱風形成區域，而颱風形成後，其主要路徑之一則為沿著太平洋副熱帶高壓南側之東

風帶往西直行朝向臺灣、亞洲大陸前進。從圖8之分析可推估，未來臺灣地區之夏季降雨增多趨勢的主要來源為臺灣東南側颱風活躍地區的降雨，且呈現線性遞增特性，這結果隱喻未來臺灣夏季將有更多颱風自臺灣東南側洋域帶來更多颱風雨進入臺灣，促使臺灣地區夏季降雨增加。Chen and Chen(2011)研究指出，臺灣夏季降雨於過去 60 年的全球暖化背景之下亦產生颱風雨偏多的趨勢，而此颱風雨增加趨勢預期於全球暖化進行的未來 100 年內，料將持續增加，而使臺灣夏季降雨呈現增加趨勢，如圖8分析結果所示。

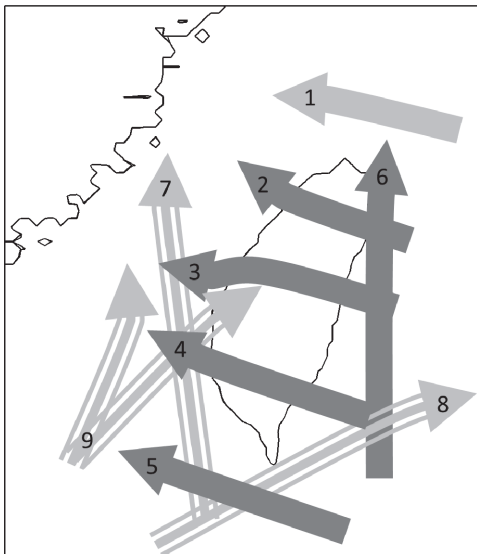


圖 7: 依中央氣象局(2006)所定義之侵臺颱風 9 種路徑。

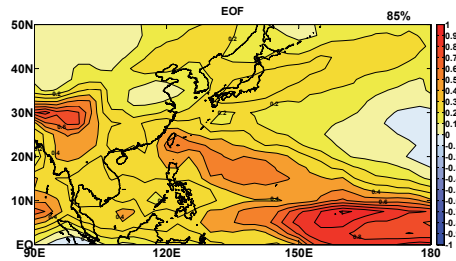
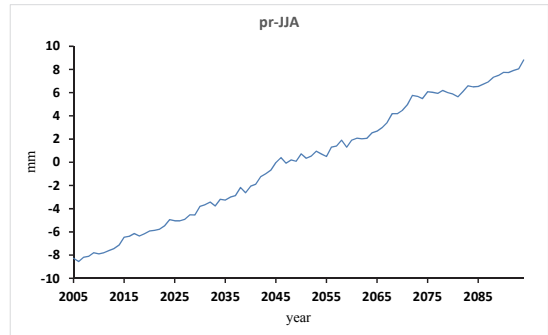


圖 8：IPCC A1B 實驗夏季降雨平均值之第一模態：
(a)時間序列(單位：mm)，(b)空間分佈圖。
此模態佔所有變異量之 85%。

六、結論

全球暖化為當前全球最熱烈討論的氣候與環境議題，其形成原因主要與人類活動所造成溫室氣體增加息息相關，且此暖化現象預期將隨著人類經濟與科技發展而持續進行。全球暖化之直接衝擊為溫度上升，間接衝擊則為全球環流變化與降雨型態改變，臺灣為一海島，主要水資源來自降雨，未來全球暖化持續進行之下，對臺灣降雨與水資源供給之影響方式為何，值得深入關心，期以協助擬定因應全球暖化之水資源調適策略。

本研究以 IPCC 所執行 2000-2100 年氣候預報實驗為分析對象，探討未來百年內臺灣夏季降雨之變化趨勢與對應型態，期以提供水資源管理單位因應之參考資訊。研究結果顯示，於

2000-2100 年間，臺灣未來夏季溫度將呈現全面(100%)增暖趨勢，其增加幅度與未來溫室氣體含量呈現線性對應關係，溫室氣體含量愈高，增暖幅度愈大。在降雨方面，未來臺灣夏季降雨約有 2/3 機率為增加趨勢，但其增加幅度與溫室氣體含量無線性對應關係。降雨特性分析結果顯示，亞洲-西太平洋地區夏季降雨增加主要呈現線性遞增趨勢，主要增加區域有二，一為國際換日線西側之熱帶暖池區域，另一為臺灣東南側之西太平洋海域，且呈現東南-西北方向延伸之雨帶，此雨帶對應該區颱風活動之主要生成區域與移動路徑，且朝向臺灣而來，隱喻未來臺灣夏季降雨增加之主要來源為西太平洋颱風活動變多，且自臺灣東南海域移入臺灣帶來更多颱風雨，而使臺灣夏季降雨於未來呈現增加趨勢，此分析結果與過去 60 年全球暖化背景之下，臺灣地區颱風雨呈現顯著增加趨勢之分析結果互為一致。

預期未來臺灣夏季之颱風活動與降雨將更為強烈，在此背景之下，颱風降雨一般而言為顯著豪大雨，易於水庫集水區造成地表沖刷、土石崩塌，而使水庫淤積。在豪大雨持續之下，水庫蓄水功能僅能容納部份雨量，大部份雨量仍為直接入海。另一水資源系統為河川水之抽取使用，但在颱風降雨期間，上游土石沖刷使河水濁度大量提升，限制淨水廠無法抽取河水運作，故其功效亦未能發揮。唯一有所助益之處為第三水資源系統之地下

水貯存，颱風降雨量雖大，但臺灣河川因中央山脈之高聳坡度，屬荒溪型河川，大量颱風雨約在數天之內均會流入海洋，使降雨滲入地下水之時間有限，使其貯存量亦受限，況且在過去臺灣超抽地下水而使地層產生明顯下陷現象，如林邊、雲林等地區，因此地下水做為水資源主要來源之選項，亦是在漸次下降。從上述分析，若是未來臺灣地區水資源須仰賴颱風雨為主要來源時，三大水資源系統：水庫、河川水、地下水，其整體功效均會降低，在此情境之下，國家宜從三大水資源系統之外，化整為零，建立小的水資源系統，例如民間的雨水貯存系統，中水的回收利用，家庭節水裝置，甚至降低自來水的漏水率等，如此方能將得來不易的颱風雨，以全島性、全面性的水資源系統善加利用，方能有效面對未來全球暖化與氣候變遷對台灣水資源的衝擊。

參考文獻

- Chen, J.-M, F.-C. Lu, S.-L. Kuo, and C.-F. Shih, 2005: Summer climate variability in Taiwan and associated large-scale processes, *J. Meteor. Soc. Japan*, 83, 499-516.
- Chen, J.-M, T. Li, and C.-F. Shih, 2008a: Asymmetry of the El Niño-spring rainfall relationship in Taiwan. *J. Meteor. Soc. Japan*, 86, 297-312.
- Chen, J.-M., F.-C. Lu, and C.-F. Shih, 2008b: The Decadal oscillation of fall temperature in Taiwan, *Terr. Atmos. Ocean. Sci.*, 19, 497-504.

- Chen, J.-M., J.-L. Chu, C.-F. Shih, and Y.-C. Tung, 2010a: Interannual variability of circulation-rainfall relationship in Taiwan during the Mei-yu season, *Int. J. Climatology*, 30, 2264-2276.
- Chen, J.-M., T. Li, and C.-F. Shih, 2010b: Tropical cyclone and monsoon induced rainfall variability in Taiwan. *J. Climate*, 23, 4107-4120.
- Chen, J.-M., and H.-S. Chen, 2011: Interdecadal Variability of Summer Rainfall in Taiwan associated with Tropical Cyclones and Monsoon, *J. Climate*, 24, 5786-5798.
- Chu, P.-S., and J.-B. Wang, 1997: Recent climate change in the tropical western Pacific and Indian Ocean region as detected by outgoing longwave radiation records. *J. Climate*, 10, 636-646.
- Emanuel, K., 2005: Increasing destructiveness of tropical cyclones over the past 30 years. *Nature*, 436, 686-688.
- Intergovernmental Panel on Climate Change, 2007: The fourth assessment report "Climate change 2007: The Physical Science Basis", 996PP.
- Intergovernmental Panel on Climate Change, 2013: The fifth assessment report "Climate Change 2013: The Physical Science Basis", 1535PP.
- Liu, S. C., C. Fu, C.-J. Shiu, J.-P. Chen, and F. Wu, 2009. Temperature dependence of global precipitation extremes, *Geophysical Research Letters*, 36, L17702, doi: 10.1029/2009GL040218.
- Oouchi, K., J. Yoshimura, H. Yoshimura, R. Mizuta, S. Kusunoki, and A. Noda, 2006: Tropical cyclone climatology in a global-warming climate as simulated in a 20 km-mesh global atmospheric model: Frequency and wind intensity analysis. *J. Meteor. Soc. Japan*, 84, 259-276.
- Webster, P. J., G. J. Holland, J. A. Curry, and H.-R. Chang, 2005: Changes in tropical cyclone number, duration and intensity in a warming environment. *Science*, 309, 1844-1846.
- Woodward, W. A., and H. L. Gray, 1993: Global warming and the problem of testing for trend in time series data. *J. Climate*, 6, 953-962.
- 中央氣象局, 2006: 氣象宣導系列合輯, 交通部中央氣象局, 112 頁。
- 許中一, 2009: 全球暖化對未來氣候、颱風、洋流之可能影響, 國立高雄海洋科技大學航海科技研究所, 碩士論文, 69 頁。
- 陳昭銘, 2006: "氣候變異", 氣象與工程系列叢書, 謝信良主編, 財團法人中興工程科技研究發展基金會發行, ISBN-13:978-986-7142-24-5, 63 頁。
- 陳昭銘、汪鳳如, 2000: 臺灣地區長期暖化現象與太平洋海溫變化之關係。 *大氣科學*, 28, 221-242.
- 經濟部水利署, 2012: 百年臺灣重大水利建設紀要, 經濟部水利署, ISBN-978-986-03-2978-0, 312 頁。

「建築水資源與給排水期刊」 徵稿資訊

Journal of Water Resource, Supply and Drainage for Buildings

本刊徵求水資源、供應與建築給水排水技術等研究領域之未刊登於其他刊物之研究論著，研究領域涵蓋：

- 降雨型態與變化特性；
- 水資源之保護、優化配置、與開源節流；
- 豪大雨預測、災害與防治；
- 建築給排水系統與設備；
- 建築機電系統與設備；
- 建築節水技術；
- 污水處理與排放；
- 健康衛生設備；
- 永續綠建築與政策；
- 符合本期刊主題技術研發新知之研究回顧。

- 一、本稿文責由作者自負，且不得侵害他人之著作權，若有相關違反學術倫理行為，經查屬實者，由作者自負法律責任。
- 二、刊登之著作，其版權屬於本刊，非徵得同意，不得轉載至其他學術期刊投稿稿件，請依下列順序書寫：封面頁(含中英文標題、作者中英文姓名、服務單位)、中英文摘要及關鍵字、本文、註釋、圖表、參考文獻及附錄。
- 三、刊登之著作，其版權屬於本刊，非徵得同意，不得轉載至其他學術期刊
- 四、投稿稿件，請依下列順序書寫：封面頁(含中英文標題、作者中英文姓名、服務單位)、中英文摘要及關鍵字、本文、註釋、圖表、參考文獻及附錄。
- 五、本文採用匿名審稿制，於收到作者稿件後委請編輯委員會送請兩位審查委員進行審查，審查委員之評審建議，原則上依下表列方式處理。若兩位審查委員對同一篇稿件之審查意見相左時，本刊將另請第三位委員審查，並綜合三位委員之審查意見處理。
- 六、為維持本刊之學術水準與公平性，本刊得將審查委員建議採納或退稿的稿件，分別作刊登或不予刊登之處理。
- 七、來稿請將稿件 Word 檔案 e-mail 至 jwrsdb@msa.hinet.net。聯絡人：祁冠慧，電話：+886-7-3718327 傳真: 886-7-3718325

建築水資源與給排水期刊 創刊號

Journal of Water Resource, Supply and Drainage for Buildings

期刊頻率：年刊

出版機關：社團法人台灣給水排水研究學會

地 址：80792 高雄市三民區鼎祥街 166 號 2 樓

網 址：<http://www.twsds.org.tw/>

電 話：(07)3718327

總 主 編：陳昭銘

主 編：楊德良、張始偉、羅德章、林呈

編審委員：趙鋌、錢梅、鄭政利、李平章、李孟杰、柯互重、談珮華、
蘇樂梅、蔣順田、謝志敏、陳本源、涂建翊、黃國倉、陳廷育、
徐銀地、吳德憲、林顯祥、蔡坤河、洪再崑、陳金保

出版年月：2015 年 2 月

創刊年月：2015 年 2 月

ISBN：978-986-91623-0-2

本著作保留所有權利，欲利用本著作全部或部份內容者，須徵求社團法人台灣給水排水研究學會書面授權。



ISBN 978-986-91623-0-2



9 789869 162302